Materials Characterization 200 (2023) 112882

Contents lists available at ScienceDirect

Materials Characterization

journal homepage: www.elsevier.com/locate/matchar

Experimental evidence of zonal dislocations in the Ti_2AlC MAX phase

Alexandre Mussi [a,**], Adrien Henzelmeier [b], Timmo Weidner [a], Marc Novelli [b,c], Yu Wenbo [d], Fabien Cuvilly [e], Thierry Grosdidier [b,c], Antoine Guitton [b,c,*]

[a] Univ. Lille, CNRS, INRAE, Centrale Lille, UMR 8207 - UMET - Unité Matériaux et Transformations, F-59000 Lille, France
[b] Université de Lorraine, CNRS, Arts et Métiers, LEM3, Metz 57070, France
[c] LabEx DAMAS, Université de Lorraine, Metz 57070, France
[d] Center of Materials Science and Engineering, School of Mechanical and Electronic Control Engineering, Beijing Jiaotong University, Beijing 100044, China
[e] Groupe de Physique des Matériaux, Normandie Université, UNIROUEN, INSA Rouen, CNRS, 76000 Rouen, France

ARTICLE INFO

Keywords:
MAX phases
Severe plastic deformation
Surface mechanical attrition treatment
Transmission electron microscopy
Dislocations

ABSTRACT

The dislocation configurations of a Ti_2AlC-MAX phase deformed under severe plastic deformation by surface mechanical attrition treatment have been analyzed by transmission electron microscopy. Results show that the microstructure of the deformed Ti_2AlC sample is composed of numerous $\langle \boldsymbol{a} \rangle$-dislocations, which interact with each other notably with dipolar configurations. In addition, we report here $\langle \boldsymbol{a} \rangle$-dislocation dissociations in the basal plane with a dissociation distance of approximately 20 nm, following the reaction $\frac{1}{3}\langle 2\bar{1}\bar{1}0 \rangle \Leftrightarrow \frac{1}{3}\langle 1\bar{1}00 \rangle + \frac{1}{3}\langle 10\bar{1}0 \rangle$. Finally, evidence of zonal dislocations is reported. These original results are discussed in the context of the fundamental deformation mechanisms of nanolayered ternary alloys.

1. Introduction

MAX phases are a unique class of materials that are stiff, lightweight, machinable, resistant to oxidation and thermal shock, and capable of remaining strong up to temperatures above 1300 °C even in air [1]. About fifty compounds were synthesized with the same range of properties. Because of their composition, these materials were named $M_{n+1}AX_n$ phases, where M stands for a transition metal; A for A-group element; X for carbon and/or nitrogen and n is an integer from 1 to 3 [1,2].

MAX phases have a laminated structure with a hexagonal lattice ($P6_3/mmc$) and a $\frac{c}{a}$ higher than 3 [3]. MAX phases exhibit a brittle-to-ductile transition around 800 °C [2,4].

MAX polycrystals, fabricated by powder metallurgy, exhibit anisotropic microstructure with grains being highly elongated in the Basal Plane (BP) direction [5]. It has been shown that the MAX polycrystal can be described as mixture of soft and hard grains leading to a high local concentration of non-uniaxial stresses at grain boundaries [6,7]. When MAX samples are subjected to load-unload cycles an intriguing behavior is observed: reversible hysteresis loops are recorded for a given loading axis [8]. This reversible hysteresis behavior can be explained by this microstructure anisotropy and the associated Bauschinger effect [9], *i.e.* within the classical framework of crystal plasticity in polycrystals [6]. Furthermore, nanoindentation experiments on single MAX phase grains seem to indicate that microstructural anisotropy cannot be solely responsible of the reversible hysteresis loops [10].

It has been argued that the formation of Kink Bands (KBs) in MAX phases is favored because mechanical twinning is excluded due to their high $\frac{c}{a}$ [11–13]. However, this paradigm must be changed because of recent evidence of $\{11\bar{2}2\}$ and $\{11\bar{2}1\}$ deformation nanotwins in nanoindented-Ti_2AlN [14]. Because of the high $\frac{c}{a}$ rendering non-basal slip is energetically costly [13,15], Room-Temperature (RT) deformation involves $\langle \boldsymbol{a} \rangle$-type dislocations ($\boldsymbol{b} = \frac{a}{3}\langle 11\bar{2}0 \rangle$) gliding in (0001) BPs as single slip [12,16], forming large pile-ups and walls [12,17]. The walls may interact to form pairs of low-angle grain boundaries (or kink boundaries) [18,19]. Concerning Stacking Faults (SFs), they were observed in numerous MAX phases, but they originate from stacking errors in the layer sequence during synthesis [20]. Basal dislocations are expected to dissociate according to the reaction: $\frac{1}{3}\langle 11\bar{2}0 \rangle \Leftrightarrow \frac{1}{3}\langle 10\bar{1}0 \rangle + \frac{1}{3}\langle 01\bar{1}0 \rangle + SF$ [15,21]. These partials are subjected to glide on BPs and they may contribute to the deformation process [20]. The value of the dissociation distance between both partials was estimated to be about 0.6 nm [21]. The Stacking Fault Energy (SFE) has been computed to be

* Corresponding author at: Université de Lorraine, CNRS, Arts et Métiers, LEM3, 7 rue Félix Savart, Metz 57070, France.
** Corresponding author at: Univ. Lille, Unité Matériaux Et Transformations - UMR CNRS 8207, Villeneuve d'Ascq Cedex 59655, France.
E-mail addresses: alexandre.mussi@univ-lille.fr (A. Mussi), antoine.guitton@univ-lorraine.fr (A. Guitton).

https://doi.org/10.1016/j.matchar.2023.112882
Received 20 January 2023; Received in revised form 29 March 2023; Accepted 31 March 2023
Available online 5 April 2023
1044-5803/© 2023 Elsevier Inc. All rights reserved.

equal to approximately 0.6 J • m^{-2} for MAX phases [15,22–24]. Additionally, numerous dislocation dipoles, alignments and nodes have been observed in RT-deformed Ti_2AlN [16]. Such dislocation reactions result in the formation of cells [16]. Dislocations have been also observed to align along specific directions leading to segments with screw, 30°, 60° or edge character, indicative of an elevated lattice friction [16,21]. In addition, out-of-basal-plane dislocations are observed in as-grown Ti_4AlN_3 [22] and in Ti_3SnC_2 [25]. At high temperature, it is observed that out-of-BP dislocations are not anecdotal events and therefore cross-slip plays a key role in the deformation [26,27]. This increase of available glide systems is likely to promote some ductility at high temperature. Note also that evidence of Frank partial ⟨***c***⟩-dislocations associated with a diffusion mechanism of Cu into Ti_2AlC has been recently reported [28].

Despite numerous characterizations of dislocation configurations in MAX phases, the majority of literature is focused on the onset of plasticity. Only few of them report detailed characterizations after substantial amount of plasticity [14,16,17,25,29]. MAX phases are brittle at RT. Thus, deformation set-ups coupled with confining pressure (gas or solid) are required to create a hydrostatic (or quasi-hydrostatic in the case of nanoindentation) confining pressure that hinders cracking and enables reaching enough plasticity.

In this paper, we bring new insights on the dislocation configurations after RT severe plastic deformation. For this, Surface Mechanical Attrition Treatment (SMAT), a Severe Plastic Deformation (SPD) technique that consists of numerous collisions of a peening media having random trajectories inside a confined chamber, has been used [30,31]. Burgers vectors and dislocation line directions are determined by Transmission Electron Microscopy (TEM).

2. Materials and methods

Fully dense Ti_2AlC was synthesized by powder metallurgy as detailed in [32]. Briefly, 99.5 wt% purity powders of Ti, Al and TiC were mixed in stoichiometric proportions and pressure less sintered at 1400 °C. An additional 10 wt% of Al was added to the initial powder mixture to compensate evaporation. Then, the surface of the specimen was severely deformed by 3 min of SMAT using 100C6 Ø2 mm spherical shots set in motion by a sonotrode vibrating at 20 kHz with an amplitude of 40 μm. Detailed characterizations of the deformed surface are presented in [33]. A thin lamella was prepared perpendicular of the SMATed surface within one grain by Focused Ion Beam (FIB) using the *in-situ* lift-out technique in a dual-beam ThermoFisher Helios PFIB G4. Then microstructure analysis was carried out on the electron microscopy facility of the Advanced Characterization Platform of the Chevreul Institute, with a FEI® Tecnai $G^2$20Twin microscope, operating at 200 kV equipped with a LaB_6 filament using Weak-Beam Dark Field (WBDF) technique and extinction diffraction condition technique. The technique of extinction diffraction condition consists in tilting the sample to select several diffraction vectors ***g*** which satisfy the relation $\boldsymbol{g} \bullet \boldsymbol{b} = 0$ [34–38]. To improve these characterizations, dislocation contrasts were analyzed considering that the contrast is linked with $\boldsymbol{g} \bullet \boldsymbol{b}$ in WBDF conditions [37] (see Supplementary Materials for more details).

3. Results

3.1. Overview of dislocation configurations

The microstructure of the Ti_2AlC specimen (see Fig. 1) comes from the cross-section of the SMATed surface (the studied grain has been selected following electron channeling contrast analyses). This microstructure is rich (dislocation density of approximately 4.3 × 10^{13} m^{-2}) and complex, it shows many dislocations in interaction. Contrasts consistent with a dipole with $\boldsymbol{a_3} = \frac{1}{3}[\bar{1}\bar{1}20]$ as Burgers vector is pointed out by two yellow arrows in the middle of Fig. 1. From the invisibility

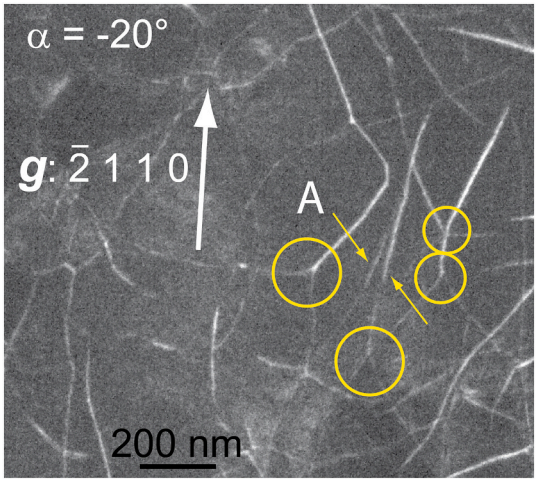

Fig. 1. WBDF micrograph, obtained with $\bar{2}$**110**, revealing the dislocation microstructure of the SMATed Ti_2AlC specimen, with a projection angle of −20°. A dislocation dipole is pointed out by two yellow arrows and four dislocation configurations (zone labelled "A") are pointed out by yellow circles. (For interpretation of the references to colour in this figure legend, the reader is referred to the web version of this article.)

and contrast criteria, both dislocations have the same Burgers vectors with opposite signs as they mutually attract each other. The acquisition of a tilt-series (54 micrographs obtained with projected angles[1] ranging from −54° to 52° every 2°) provides to an accurate measurement of the distance between both dislocations (see Supplementary Materials). Note that this distance is roughly estimated since the position of the dislocation intensity peak of a WBDF micrograph is different from the real dislocation core position [38]. This resulting distance is 37.5 ± 2.5 nm (the uncertainty has been obtained considering the curve thickness in Supplementary Materials).

Fig. 2 is a detailed zone of the center of Fig. 1 (we focus on the circle located on the far left) obtained for several diffraction vectors. Six WBDF micrographs obtained with six specific diffraction vectors are shown in Fig. 2 (the tilt-series has been acquired with $\boldsymbol{g_1} = (\bar{2}110)$). These micrographs allow to determine Burgers vectors. Table 1 gives access to the different values of $|\boldsymbol{g} \bullet \boldsymbol{b}|$ for the six ***g*** and the expected ***b*** in MAX phases [16,19].

3.2. Dislocation dissociations

The first configuration analyzed in this work is localized by the letter "B" in Fig. 2.a. It will be referenced as "*B zone*". This configuration is composed of two parallel segments of dislocations. They are separated by 19.7 ± 0.8 nm between both dislocations. This is lower than the presumed dislocation dipole distance previously measured (37.5 ± 2.5 nm), thus suggesting a dislocation dissociation, while two partial dislocations can be distinguished in Fig. 2.a; only one partial is visible in Fig. 2.b; and the other partial one in Fig. 2.c. From Table 1, $|\boldsymbol{g} \bullet \boldsymbol{b}|$ is equal to 1 with $\boldsymbol{g_1}$ (diffraction condition of Fig. 2.a) for the two partials $\boldsymbol{p_2} = \frac{1}{3}[10\bar{1}0]$ and $\boldsymbol{p_3} = \frac{1}{3}[1\bar{1}00]$; comparatively, $|\boldsymbol{g} \bullet \boldsymbol{b}|$ is equal to 0 with $\boldsymbol{g_2}$ (diffraction condition of Fig. 2.b) for the partial $\boldsymbol{p_2}$ and equal to 1 for the partial $\boldsymbol{p_3}$, while it is equal to 1 with $\boldsymbol{g_3}$ (diffraction condition of Fig. 2.c) for the partial $\boldsymbol{p_2}$ and equal to 0 for the partial $\boldsymbol{p_3}$. Therefore, the dissociation reaction is consistent with:

$$\boldsymbol{a_1} \Leftrightarrow \boldsymbol{p_2} + \boldsymbol{p_3} + SF \quad (1)$$

[1] A projection angle corresponds to the angle between the electron beam direction and the normal of the thin foil for a given tilt angle.

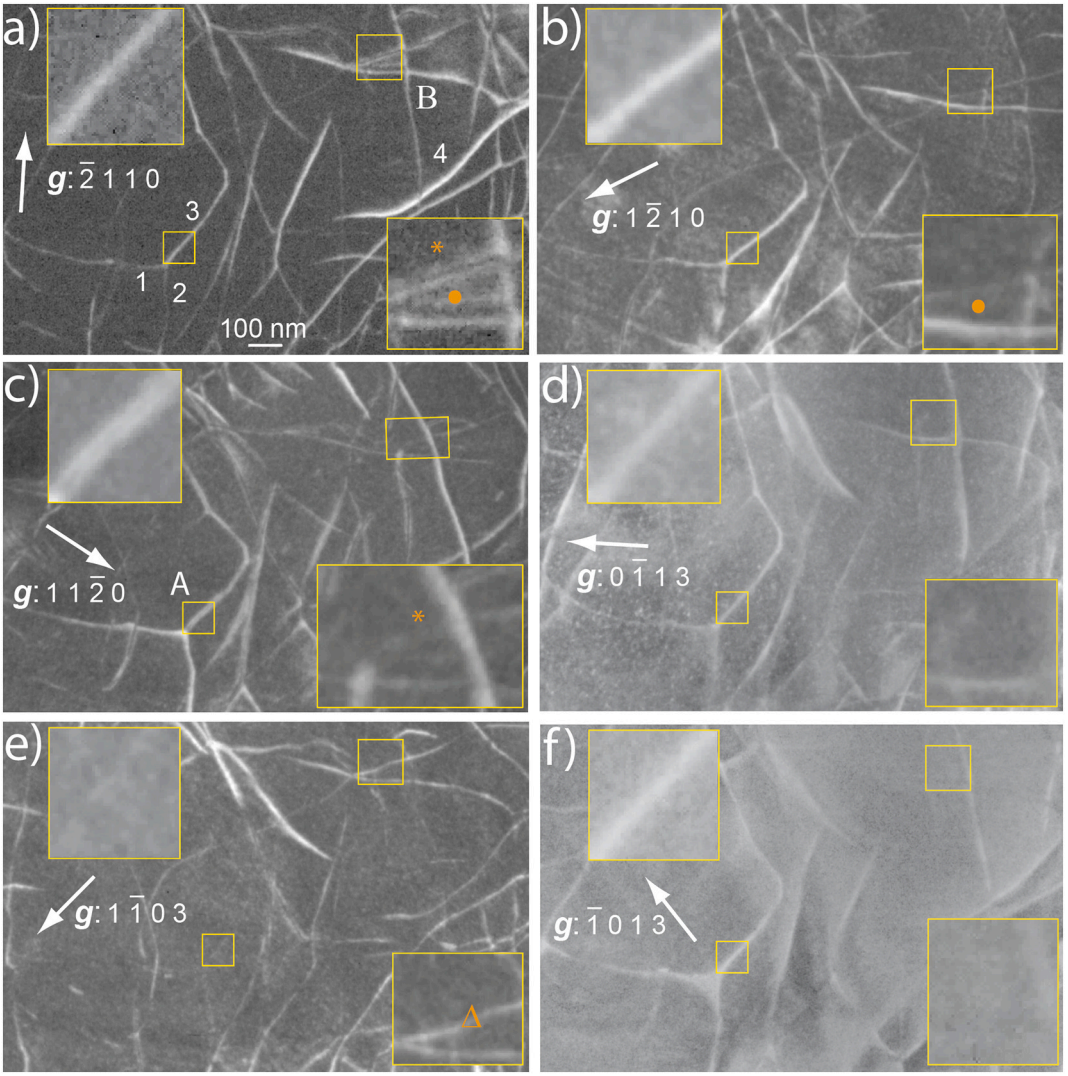

Fig. 2. Indexations of Burgers vectors. (a) WBDF micrograph obtained with $\bar{2}110$: the contrast of dislocation 4 is high, medium for dislocation 3, and weak contrast for dislocations 1 and 2; both partial dislocations of a dissociated dislocation (indicated by the letter "B") are in contrast (pointed out by an orange asterisk and an orange disk); (b) WBDF micrograph obtained with $1\bar{2}10$: only the partial dislocation pointed out by an orange disk is in contrast; (c) WBDF micrograph obtained with $11\bar{2}0$: only the partial dislocation pointed out by an orange asterisk is in contrast, and two partial dislocations are noted on dislocation 3 (indicated by the letter "A"); (d) WBDF micrograph obtained with $0\bar{1}13$: dislocations 1, 2 and 3 are in contrast and dislocation 4 is out of contrast; both partial dislocations pointed out by the letter "B" on (a) are out of contrast; (e) WBDF micrograph obtained with $1\bar{1}03$: dislocations 1, 2 and 3 are out of contrast and dislocation 4 is in contrast; both partial dislocations pointed out by the letter "B" on (a) are out of contrast, but only the stacking fault is in contrast (pointed out by an orange triangle); (f) WBDF micrograph obtained with $\bar{1}013$: dislocations 1, 2 and 3 are in contrast and an extended node is noticeable between these dislocations; both partial dislocations pointed out by the letter "B" on (a) are out of contrast. Zooms of dislocation 3 and zone "B" (pointed out by a yellow squares) are done on each micrograph. (For interpretation of the references to colour in this figure legend, the reader is referred to the web version of this article.)

Table 1
$|\boldsymbol{g} \bullet \boldsymbol{b}|$ for the six diffraction vectors used in this study.

$\lvert \boldsymbol{g} \bullet \boldsymbol{b} \rvert$	$\boldsymbol{g}_1 = (\bar{2}110)$	$\boldsymbol{g}_2 = (1\bar{2}10)$	$\boldsymbol{g}_3 = (11\bar{2}0)$	$\boldsymbol{g}_4 = (0\bar{1}13)$	$\boldsymbol{g}_5 = (1\bar{1}03)$	$\boldsymbol{g}_6 = (\bar{1}013)$
$\boldsymbol{a}_1 = \frac{1}{3}[2\bar{1}\bar{1}0]$	2	1	1	0	1	1
$\boldsymbol{a}_2 = \frac{1}{3}[\bar{1}2\bar{1}0]$	1	2	1	1	1	0
$\boldsymbol{a}_3 = \frac{1}{3}[\bar{1}\bar{1}20]$	1	1	2	1	0	1
$\boldsymbol{p}_1 = \frac{1}{3}[01\bar{1}0]$	0	1	1	$\frac{2}{3}$	$\frac{1}{3}$	$\frac{1}{3}$
$\boldsymbol{p}_2 = \frac{1}{3}[10\bar{1}0]$	1	0	1	$\frac{1}{3}$	$\frac{1}{3}$	$\frac{2}{3}$
$\boldsymbol{p}_3 = \frac{1}{3}[1\bar{1}00]$	1	1	0	$\frac{1}{3}$	$\frac{2}{3}$	$\frac{1}{3}$

Since the plastic deformation of MAX phases operates predominantly through the glide of $\frac{1}{3}\langle 2\bar{1}\bar{1}0\rangle$ dislocations on basal planes [16,18,20], their dissociations occur in basal planes as well [21]. Indeed, the direction of the dislocation line is along $\boldsymbol{u} = [\bar{1}2\bar{1}0]$ *i.e.* edge for $\boldsymbol{p_2}$, mixed with 30°character for $\boldsymbol{p_3}$ and mixed with 60° character for $\boldsymbol{a_1}$.

Using the same methodology, Fig. 2 shows another dissociation reaction (pointed out with a white letter "A" in Fig. 2.c):

$$\boldsymbol{a_3} \Leftrightarrow \boldsymbol{p_1} + \boldsymbol{p_2} + SF \quad (2)$$

It will be referenced as "*A zone*". Only one partial is visible in Fig. 2.a (diffraction condition: $\boldsymbol{g_1}$); the other partial in Fig. 2.b (diffraction condition: $\boldsymbol{g_2}$); and the two partials in Fig. 2.c (diffraction condition: $\boldsymbol{g_3}$). Considering the difference in contrasts in Fig. 2, note *a priori* that the partials (labeled 1 and 2) of the A zone tend to split up. By looking at values of $|\boldsymbol{g} \bullet \boldsymbol{b}|$ for $\boldsymbol{g_1}$ (see Table 1), several interpretations can be made: (*i*) $|\boldsymbol{g} \bullet \boldsymbol{b}|$ will be equal to 0, if partials $\boldsymbol{p_1}$ are assumed; (*ii*) those products will become equal to 1, if either partials $\boldsymbol{p_2}$ and $\boldsymbol{p_3}$ or perfects $\boldsymbol{a_2}$ and $\boldsymbol{a_3}$ are considered; (*iii*) they will be equal to 2, if perfect dislocations $\boldsymbol{a_1}$ are expected. To summarize, there would be two different contrasts (ignoring the configuration where dislocations are out of contrast) on WBDF micrographs obtained with $\boldsymbol{g_1}$.

Fig. 3 is an analysis of dislocation contrasts observed in the region of interest. Table 2 provides the value of the intensity peak I of the dislocations labelled 1, 2, 3 and 4 (see Fig. 3) averaged over the tilt-series. The WBDF conditions, obtained with diffraction vector $\boldsymbol{g_1}$, are precisely maintained all over the tilt-series, as performed in previous works [40–42], perfectly aligning $\boldsymbol{g_1}$ with the principal axis of the sample-holder (*i.e.* the tilt axis). Three contrasts are clearly identified, since dislocations labelled 1 and 2 are weakly contrasted (the average value of

Table 2
Intensity peak maximums (averaged over 50 profiles) of the four dislocations labelled on Fig. 2 and Fig. 3, for several micrographs extracted from the tilt-series (the intensity peak maximum of dislocation 4 is fixed at 16).

Extracted Micrographs From the tilt-series	Dislocation 1 I / $\sqrt{I}$ (a.u.)	Dislocation 2 I / $\sqrt{I}$ (a.u.)	Dislocation 3 I / $\sqrt{I}$ (a.u.)	Dislocation 4 I / $\sqrt{I}$ (a.u.)
−30°	0.9 / 1.0	1.0 / 1.0	4.6 / 2.2	16 / 4
−16°	1.2 / 1.1	0.9 / 0.9	4.8 / 2.2	16 / 4
−12°	1.3 / 1.1	0.7 / 0.8	4.2 / 2.0	16 / 4
−2°	1.3 / 1.1	0.7 / 0.8	3.1 / 1.8	16 / 4
8°	1.4 / 1.2	0.9 / 0.9	4.8 / 2.2	16 / 4
26°	1.4 / 1.2	0.9 / 1.0	3.6 / 1.9	16 / 4

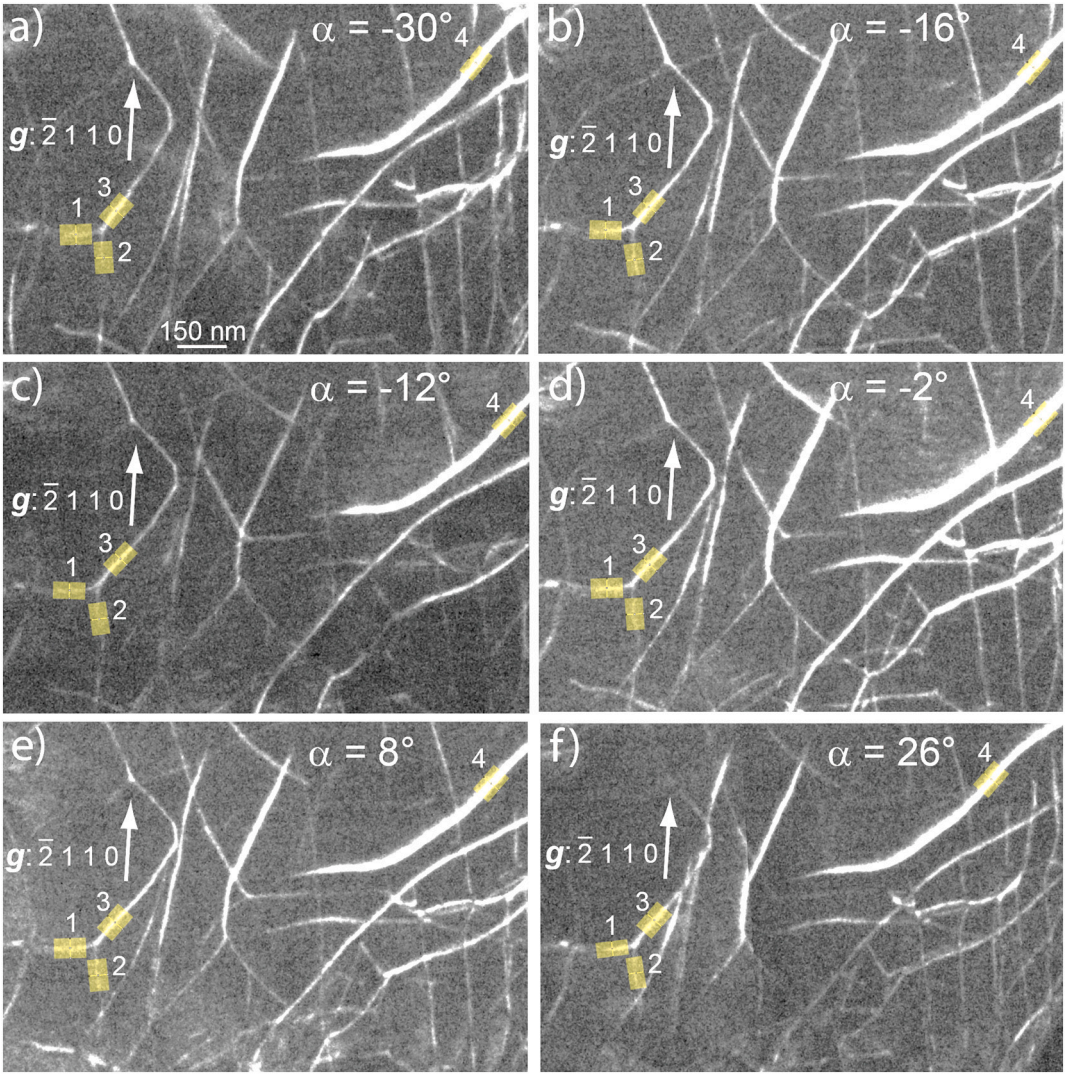

Fig. 3. Contrast analyses of dislocations 1, 2, 3 and 4 (obtained with the sum of 50 profiles) in WBDF condition with $\bar{2}\mathbf{110}$ for a: (a) projection angle of −30°; (b) projection angle of −16°; (c) projection angle of −12°; (d) projection angle of −2°; (e) projection angle of 8°; (f) and a projection angle of 26°. Each intensity is indicated in Table 2.

$\sqrt{I}$ is 1); dislocation labelled 3 has a medium contrast (the average value of $\sqrt{I}$ is 2); and the dislocation labelled 4 is highly contrasted (the average value of $\sqrt{I}$ is 4).

Moreover, a SF should be spread between dislocations 1 and 2 if they were partials. But, from Fig. 2.f (diffraction condition: $\boldsymbol{g_6}$), it can be clearly noticed an extended node between dislocations 1, 2 and 3. Additionally, using the invisibility and contrast criteria on dislocations 1 and 2, such dislocations are perfect with $\boldsymbol{a_3}$ as Burgers vector (Fig. 2), as they are both in contrast with $\boldsymbol{g_1}$, $\boldsymbol{g_2}$ and $\boldsymbol{g_3}$ (with a higher contrast for $\boldsymbol{g_3}$), and out of contrast with $\boldsymbol{g_5}$ (see Table 1). Note that several similar configurations are identified (see yellow circles on Fig. 1).

4. Discussion

TEM micrographs unambiguously show that Ti_2AlC was successfully plastically deformed. The wide varieties of dislocation directions and configurations are due to the solid confining pressure that closes cracks to the favor of the plasticity during SMAT [5,16]. Note that, under room-pressure condition, only the rise in temperature enables reaching significant plasticity before intergranular failure [26,39]. Our TEM observations reveal that numerous dislocation interactions exist. More precisely, some configurations correspond to $\langle \boldsymbol{a} \rangle$-dislocation dipoles, already reported in MAX phases [15] and $\langle \boldsymbol{a} \rangle$-dislocation dissociations following the reaction $\frac{1}{3}\langle 2\bar{1}\bar{1}0\rangle \Leftrightarrow \frac{1}{3}\langle 1\bar{1}00\rangle + \frac{1}{3}\langle 10\bar{1}0\rangle + SF$, as already reported in [23].

As mentioned earlier, the separation distance between both partials in the C zone is estimated to be equal to 19.7 ± 0.8 nm (see letter "C" on Fig. 2.a). This distance is out of the range of the calculated one reported in [21], which was estimated equal to ~0.6 nm. It is below the resolution of conventional TEM, where the resolution in WBDF is of the order of few nm. Therefore, both partials appear as one perfect dislocation. An explanation for this wider separation can originate in the fact that calculations in [21] were carried out at 0 K, far from the current experimental conditions. Although SMAT was carried out at RT, at the surface it is well established that there is some temperature rise due to the impact of the colliding media [43,44]. Local temperature rising has been modelled and estimated as high as 200 °C under the impact where deformation occurs [42]. Note that we neglect a possible Suzuki effect [45]. From this separation distance between both partials, it is possible to calculate the SFE (see Supplementary Materials). It gives: ~53 mJ • m^{-2}. Note that this value is a rough estimation, since the tilt parameter (ω) is here lower than 5 ($\omega = 3.8$), thus giving a non-quantitative value of the SFE [38,46]. Nevertheless, it has the advantage of providing an order of magnitude.

Concerning the second dissociation observed in Fig. 2 (see letter "A") or in Fig. 3, the observed contrasts are not consistent with a simple configuration of partials. Such configuration can be described as Basal Dislocation Pair (BDP), where dissociations occur on BPs. Fig. 4 schematizes this configuration: two $\boldsymbol{a_3}$-perfect dislocations (labelled $\boldsymbol{a_3}$ and $\boldsymbol{a'_3}$ in Fig. 4) are lying in two successive BPs (labelled (*B*) in Fig. 4), thus forming a BDP. Each $\boldsymbol{a_3}$ dislocation dissociates into two partials $\boldsymbol{p_1}$ and $\boldsymbol{p_2}$, both lying in their respective BPs (*B*). This results in the two couples $\{\boldsymbol{p_1};\boldsymbol{p'_1}\}$ on one hand, and $\{\boldsymbol{p_2};\boldsymbol{p'_2}\}$ on the other hand, are stacked on top of one another. Which can also be viewed as two zonal dislocations [15,47,48]. Such zonal dislocations were predicted in MAX phases by Plummer et al. [15], but they have not yet been reported experimentally in MAX phases. In addition, Plummer et al. concluded that BDP dissociates as zonal dislocations over much larger distances compared with *normal* dissociation into partials [15], thus making them visible here by TEM. Then, the $\boldsymbol{a_3}$ dislocation crosses slip from the (*B*)-plane into another plan (*P*)-plane, while $\boldsymbol{a'_3}$ remains on its (*B*)-plane. Note that cross-slip of $\langle \boldsymbol{a} \rangle$-dislocations was already reported in the Ti_2AlN MAX phase deformed at 900 °C [26]. Finally, since both $\{\boldsymbol{a_3};\boldsymbol{a'_3}\}$ are not in zonal configuration anymore, their dissociation into $\boldsymbol{p_1} + \boldsymbol{p_2}$ (or $\boldsymbol{p'_1} + \boldsymbol{p'_2}$) is not detectable by TEM, as discussed in [21].

5. Conclusions

The large amounts of plastic strain reachable by this SPD technique gives access to original microstructures never observed before for MAX phases. In conclusion, the deformation microstructure of SMATed Ti_2AlC was studied, giving new insights into the deformation mechanisms.

Numerous dislocation interactions, such as presumed dipoles and dissociations of $\langle \boldsymbol{a} \rangle$-dislocations were characterized. Moreover, evidence of zonal dislocations was brought. Interestingly, mechanical twinning was recently reported in MAX phases [14]. In addition, in several materials, some mechanisms suggest that mechanical twinning and zonal dislocations are strongly related to each other [47–50], and zonal dislocations can be viewed as the embryos of mechanical twinning. Such outcomes should be considered in the comprehension of the fundamental deformation mechanisms of MAX phases and more generally of nanolayered materials.

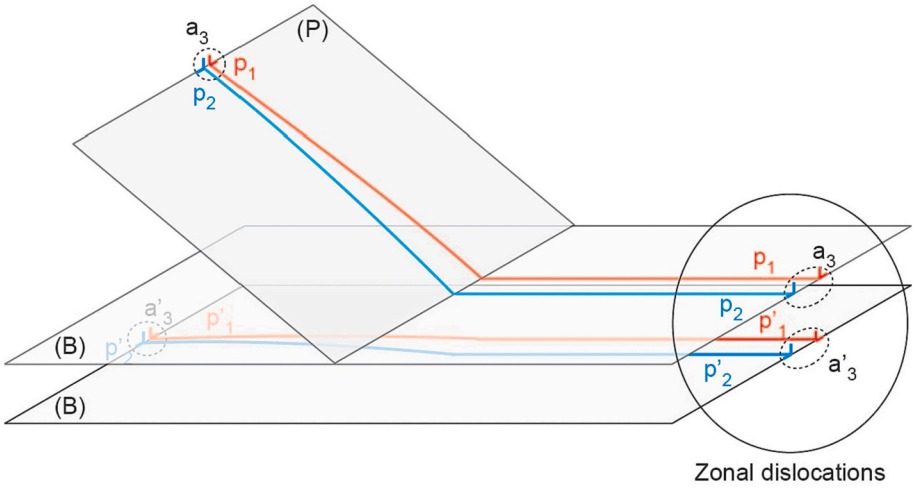

Fig. 4. Schematic of the dissociation configuration (A zone) characterized in Fig. 2. (***B***) stands for basal plane and (***P***) for a non-basal plane. $\boldsymbol{a_3}$ and $\boldsymbol{a'_3}$ are the two perfect dislocations, thus forming a BDP. They will dissociate into two partials: $\boldsymbol{p_1} + \boldsymbol{p_2}$ and into $\boldsymbol{p'_1} + \boldsymbol{p'_2}$ respectively. The two couples $\{\boldsymbol{p_1};\boldsymbol{p'_1}\}$ and $\{\boldsymbol{p_2};\boldsymbol{p'_2}\}$ are zonal dislocations. Then $\boldsymbol{a_3}$ crosses slip into (***P***), while $\boldsymbol{a'_3}$ remains lying (***B***).

Declaration of Competing Interest

The authors declare that they have no known competing financial interests or personal relationships that could have appeared to influence the work reported in this paper.

Data availability

Data will be made available on request.

Acknowledgments

The TEM national facility in Lille (France) is supported by the Conseil Régional du Nord-Pas de Calais, the European Regional Development Fund (ERDF), and the Institut National des Sciences de l'Univers (INSU, CNRS). This project has received funding from the CNRS through the MITI interdisciplinary programs and from the National Natural Science Foundation of China (no. 52175284).

Appendix A. Supplementary data

Supplementary data to this article can be found online at https://doi.org/10.1016/j.matchar.2023.112882.

References

[1] M.W. Barsoum, T. El-Raghy, The MAX phases: unique new carbide and nitride materials, Am. Sci. 89 (2001) 334.
[2] M.W. Barsoum, The $M_{n+1}AX_n$ phases: a new class of solids, Prog. Solid State Chem. 28 (2000) 201–281.
[3] M.W. Barsoum, M. Radovic, Elastic and mechanical properties of the MAX phases, Annu. Rev. Mater. Res. 41 (2011) 195–227.
[4] Z.F. Zhang, Z.M. Sun, Shear fracture behavior of Ti_3SiC_2 induced by compression at temperatures below 1000°C, Mater. Sci. Eng. A 408 (2005) 64–71.
[5] G.-P. Bei, et al., Pressure-enforced plasticity in MAX phases: from single grain to polycrystal investigation, Philos. Mag. 93 (2013) 1784–1801.
[6] A. Guitton, S. Van Petegem, C. Tromas, A. Joulain, H. Van Swygenhoven, L. Thilly, Effect of microstructure anisotropy on the deformation of MAX polycrystals studied by in-situ compression combined with neutron diffraction, Appl. Phys. Lett. 104 (2014), 241910.
[7] N.G. Jones, et al., On the relevance of kinking to reversible hysteresis in MAX phases, Acta Mater. 69 (2014) 149–161.
[8] M.W. Barsoum, T. Zhen, S.R. Kalidindi, M. Radovic, A. Murugaiah, Fully reversible, dislocation-based compressive deformation of Ti_3SiC_2 to 1 GPa, Nat. Mater. 2 (2003) 107–111.
[9] J. Bauschinger, Ueber die Veraenderung der Elastizitaetsgrenze und des Elastizitaetsmoduls verschiedener Metalle, Zivilingenieur 27 (1881) 289–348.
[10] J. Griggs, C. Lang, J. Gruber, G.J. Tucker, M.L. Taheri, M.W. Baarsoum, Spherical nanoindentation, modeling and transmission electron microscopy evidence for ripplocations, Acta Mater. 131 (2017) 141–155.
[11] M.W. Barsoum, M. Radovic, P. Finkel, T. El-Raghy, Ti3SiC2 and ice, Appl. Phys. Lett. 79 (2001) 479–481.
[12] M.W. Barsoum, M. Radovic, Mechanical Properties of the MAX Phases, Elsevier, 2004.
[13] S. Basu, M.W. Barsoum, S.R. Kalidindi, Sapphire: a kinking nonlinear elastic solid, J. Appl. Phys. 99 (2006) 63501–63507.
[14] C. Tromas, et al., Nanoindentation-induced deformation twinning in MAX phase Ti_2AlN, Acta Mater. 227 (2022), 117665.
[15] G. Plummer, M.W. Barsoum, C.R. Weinberger, G.J. Tucker, Basal dislocations in MAX phases: Core structure and mobility, Materialia 21 (2022), 101310.
[16] A. Guitton, A. Joulain, L. Thilly, C. Tromas, Dislocation analysis of Ti_2AlN deformed at room temperature under confining pressure, Philos. Mag. 92 (2012) 4536–4546.
[17] G.P. Bei, V. Gauthier-Brunet, C. Tromas, S. Dubois, Synthesis, characterization, and intrinsic hardness of layered Nanolaminate Ti_3AlC_2 and $Ti_3Al_{0.8}Sn_{0.2}C_2$ solid solution, J. Am. Ceram. Soc. 95 (2012) 102–107.
[18] M.W. Barsoum, L. Farber, T. El-Raghy, Dislocations, kink bands, and room-temperature plasticity of Ti_3SiC_2, Metall. Mater. Trans. A 30 (1999) 1727–1738.
[19] L. Farber, I. Levin, M.W. Barsoum, High-resolution transmission electron microscopy study of a low-angle boundary in plastically deformed Ti_3SiC_2, Philos. Mag. Lett. 79 (1998) 163–1700.
[20] L. Farber, M.W. Barsoum, A. Zavaliangos, T. El-Raghy, I. Levin, Dislocations and stacking faults in Ti_3SiC_2, J. Am. Ceram. Soc. 8 (1998) 1677–1681.
[21] K. Gouriet, et al., Dislocation modelling in Ti_2AlN MAX phase based on the Peierls–Nabarro model, Philos. Mag. 95 (2015) 2539–2552.
[22] A. Joulain, L. Thilly, J. Rabier, Revisiting the defect structure of MAX phases: the case of Ti_4AlN_3, Philos. Mag. 88 (2008) 1307–1320.
[23] M. Higashi, S. Momono, K. Kishida, N.L. Okamoto, H. Inui, Anisotropic plastic deformation of single crystals of the MAX phase compound Ti_3SiC_2 investigated by micropillar compression, Acta Mater. 161 (2018) 161–170.
[24] R. Hossain, H. Kimizuka, Y. Shiihara, S. Ogata, Core structure and Peierls barrier of basal edge dislocations in Ti_3Al_2C MAX phase, Comp. Mater. Sci. 209 (2022), 111366.
[25] C. Tromas, P. Villechaise, V. Gauthier-Brunet, S. Dubois, Slip line analysis around nanoindentation imprints in Ti_3SnC_2 : a new insight into plasticity of MAX-phase materials, Philos. Mag. 91 (2011) 1265–1275.
[26] A. Guitton, A. Joulain, L. Thilly, C. Tromas, Evidence of dislocation cross-slip in MAX phase deformed at high temperature, Sci. Rep. 4 (2015) 6358.
[27] J. Guénolé, V. Taupin, M. Vallet, W. Yu, A. Guitton, Features of a nano-twist phase in the nanolayered Ti_3AlC_2 MAX phase, Scr. Mater. 210 (2022), 114425.
[28] W. Yu, J. Guénolé, J. Ghanbaja, M. Vallet, A. Guitton, Frank partial dislocation in Ti_2AlC-MAX phase induced by matrix-cu diffusion, Scr. Mater. 191 (2021) 34–39.
[29] C. Tromas, N. Ouabadi, V. Gauthier-Brunet, M. Jaouen, S. Dubois, Mechanical properties of nanolaminate Ti_3SnC_2 carbide determined by nanohardness cartography, J. Am. Ceram. Soc. 93 (2010) 330–333.
[30] T. Grosdidier, M. Novelli, Recent developments in the application of surface mechanical attrition treatments for improved gradient structures: processing parameters and surface reactivity, Mater. Trans. 60 (2019) 1344–1355.
[31] P. Maurel, L. Weiss, P. Bocher, T. Grosdidier, Effects of SMAT at cryogenic and room temperatures on the kink band and martensite formations with associated fatigue resistance in a β-metastable titanium alloy, Mater. Sci. Eng. A 803 (2021), 140618.
[32] W. Yu, M. Vallet, B. Levraut, V. Gauthier-Brunet, S. Dubois, Oxidation mechanisms in bulk Ti_2AlC: influence of the grain size, J. Eur. Ceram. Soc. 40 (2020) 1820–1828.
[33] A. Heinzelmeier, A. Guitton, M. Novelli, W. Yu, T. Grosdidier, Improving embrittlement in the Ti-Al-C MAX phase system: A composite approach for surface severe plastic deformation, J. Alloys and Comp. (2023), 169946.
[34] D.B. Williams, C.B. Carter, Transmission Electron Microscopy, Springer US, Boston, MA, 2009.
[35] J.W. Edington, Practical Electron Microscopy in Materials Science, Techbooks, 1991.
[36] D.J.H. Cockayne, I.L.F. Ray, M.J. Whelan, Investigations of dislocation strain fields using weak beams, Philos. Mag. 20 (1969) 1265–1270.
[37] R. De Ridder, S. Amelinckx, Approximate theoretical treatment of weak-beam dislocation images, Phys. Status Solidi 43 (1971) 541–550.
[38] D.J.H. Cockayne, A theoretical analysis of the weak-beam method of Electron microscopy, Z. Naturforsch. A 27 (1972) 452–460.
[39] E. Drouelle, et al., Deformation mechanisms during high temperature tensile creep of Ti_3AlC_2 MAX phase, J. Alloys Compd. 693 (2017) 622–630.
[40] A. Mussi, P. Cordier, S. Demouchy, C. Vanmansart, Characterization of the glide planes of the [001] screw dislocations in olivine using electron tomography, Phys. Chem. Miner. 41 (2014) 537–541.
[41] A. Mussi, J. Gallet, O. Castelnau, P. Cordier, Application of electron tomography of dislocations in beam-sensitive quartz to the determination of strain components, Tectonophysics 803 (2021), 228754.
[42] A. Mussi, P. Carrez, K. Gouriet, B. Hue, P. Cordier, 4D electron tomography of dislocations undergoing electron irradiation, C. R. Phys. 22 (S3) (2021) 67–81.
[43] M. Novelli, P. Bocher, T. Grosdidier, Effect of cryogenic temperatures and processing parameters on gradient-structure of a stainless steel treated by ultrasonic surface mechanical attrition treatment, Mater. Charact. 139 (2018) 197–207.
[44] S. Rouquette, E. Rouhaud, M. François, A. Roos, J.-L. Chaboche, Coupled thermo-mechanical simulations of shot impacts: effects of the temperature on the residual stress field due to shot-peening, J. Mater. Process. Technol. 209 (2009) 3879–3886.
[45] H. Suzuki, Segregation of solute atoms to stacking faults, J. Phys. Soc. Jpn. 17 (1962) 322–325.
[46] P. Pirouz, D.J.H. Cockayne, N. Sumida, P. Hirsh, A.R. Lang, Dissociation of dislocations in diamond, Proc. R. Soc. Lond. A. Math. Phys. Sci. 386 (1983) 241–249.
[47] S. Mendelson, Zonal dislocations and twin lamellae in h.c.p. metals, Mater. Sci. Eng. A 4 (1969) 231–242.
[48] B. Li, E. Ma, Zonal dislocations mediating {10−11} ⟨10−1−2⟩ twinning in magnesium, Acta Mater. 57 (2009) 1734–1743.
[49] S. Mendelson, Zonal dislocations and dislocation reactions with twins in h.c.p. metals, Scr. Metall. 4 (1970) 5–8.
[50] M.H. Yoo, Reply to 'zonal dislocations and dislocation reactions with twins in hexagonal-close-packed metals', Scr. Metall. 4 (1970) 9–11.